ELSEVIER

Contents lists available at ScienceDirect

# Chemical Engineering Journal

journal homepage: www.elsevier.com/locate/cej





# Zn-0.4Li alloy shows great potential for the fixation and healing of bone fractures at load-bearing sites

Hongtao Yang  $^{a,e,1}$ , Xinhua Qu $^{b,f,1}$ , Minqi Wang  $^{b,f}$ , Houwen Cheng  $^c$ , Bo Jia  $^{b,g}$ , Jianfeng Nie  $^{d,*}$ , Kerong Dai  $^{b,*}$ , Yufeng Zheng  $^{a,h,*}$ 

- a Department of Materials Science and Engineering, College of Engineering, Peking University, Beijing 100871, China
- b Department of Orthopedics, Shanghai Key Laboratory of Orthopedic Implant, Shanghai Ninth People's Hospital, Shanghai Jiaotong University School of Medicine, Shanghai 200011. China
- <sup>c</sup> College of Materials Science and Engineering, Chongqing University, Chongqing 400044, China
- <sup>d</sup> Department of Materials Science and Engineering, Monash University, Victoria 3800, Australia
- <sup>e</sup> School of Medical Science and Engineering, Beihang University, Beijing, 100191, China
- f Department of Bone and Joint Surgery, Renji Hospital, School of Medicine, Shanghai Jiao Tong University, Shanghai 200127, China
- g Department of Orthopedics, Shanghai General Hospital, Shanghai Jiao Tong University School of Medicine, Shanghai 200080, China
- h International Research Organization for Advanced Science and Technology, Kumamoto University, 2-39-1 Kurokami, Chuo-Ku, Kumamoto 860-8555, Japan

#### ARTICLE INFO

#### Keywords: Biodegradable Zn-Li alloys Orthopedic implants Load-bearing Osteogenesis

#### ABSTRACT

Biodegradable orthopedic implants, designed to promote vigorous bone healing and be safely absorbed by the body, are developing rapidly to complement the deficiency of conventional implants. Limited strength, however, has blocked their path to high load-bearing applications. In this study, we report a pioneering application of implants made of high-strength biodegradable Zn-Li alloy in a high load-bearing rabbit shift fracture model. The Zn-0.4Li based bone plates and screws showed comparable performance in bone fracture fixation compared to the Ti-6Al-4 V counterpart. The fracture was healed completely after 6 months. The osteogenic activity of Zn-0.4Li alloy, as a result of biodegradation, was verified in a rat femur model. Furthermore, the underlying mechanism could include activation of the PI3K-AKT pathway and stimulation of metallothionein proteins. The empirical findings here reveal the great potential of Zn-Li based alloys for degradable biomaterials in high load-bearing applications.

#### 1. Introduction

Traditional orthopedic metallic implants such as stainless steel, cobalt-chromium alloys, and titanium-based alloys are primarily designed as mechanical devices; their high strength and acceptable biosafety enable their use as major orthopedic devices in load-bearing applications [1]. However, there are known limitations to such implants. First, their long-term existence will result in the accumulation of detrimental elements like Ni, Co, Cr, Al, and V in the human body, which cause chronic inflammation and eventually lead to revisionary surgeries [2]. Second, the mismatch of the high elastic modulus between the implants and human bone will cause bone resorption and implant failure over the long run [3,4]. Third, their bioinert feature no longer fulfills the clinical demand for controllable host response and fast bone healing [5].

The revolutionary concept of biodegradable implants is brought to address these issues. Research on synthetic biodegradable polymers started in the 1960 s. Biodegradable polymers such as polyglycolide (PGA), polylactide (PLA), and poly (L- or D, L-lactic acid) (PLLA/PDLLA) have been approved by FDA for applications in orthopedic fixation implants after 60 years' development [6]. However, their applications have been limited to low load-bearing skeletal sites due to their inadequate strength. Also, the acidic degradation products produced during bulk erosion of biodegradable polymers may induce a noninfectious inflammatory reaction, ultimately leading to bone resorption [7]. More recently, developments on biodegradable magnesium (Mg)-based implants provide scientists and clinicians with new options to solve the flaws in current commercialized orthopedic implants. As biodegradable metals, Mg-based materials offer better mechanical support than their

<sup>\*</sup> Corresponding authors at: Department of Materials Science and Engineering, College of Engineering, Peking University, Beijing 100871, China (Y. Zheng): Department of Materials Science and Engineering, Monash University, Victoria 3800, Australia (J. Nie).

E-mail addresses: jianfeng.nie@monash.edu (J. Nie), krdai@163.com (K. Dai), yfzheng@pku.edu.cn (Y. Zheng).

 $<sup>^{1}\,</sup>$  These two authors contributed equally to this study.

polymer counterparts, exhibiting a desirable elastic modulus close to that of human bone tissues. More importantly, the degradation of Mg releases beneficial products such as Mg ions to promote bone regeneration and accelerate bone healing [8]. Enormous efforts on the basic research have advanced Mg to the clinical trials and commercialization in Europe [9], Korea [10], and China [11], however, their applications are still limited to fixation of fractures of non-load-bearing bones and bone fragments. Meanwhile, the unfavorable degradation mode of Mg, which produces gas cavities during fast degradation, needs to be improved in the future [11]. As a result, no biodegradable implants are capable to be applied to high load-bearing applications. Recently, our group has conducted a systematic evaluation of biodegradable zinc (Zn) alloys as orthopedic implants [12]. The results indicated that Zn-Li, Zn-Mg, Zn-Ca, and Zn-Sr alloy systems were the most desirable candidates for bone implants. Among them, Zn-Li alloys performed the comparable strength to commercially pure titanium and stainless steel, showing their potential to be used as high load-bearing implants. More recently, the development of clinical needs requires positive interaction between the host tissue and the implants, which promotes the bone regeneration and healing process. Our study found that Zn-Li alloy implants exhibited a favorable effect on promoting new bone formation. Zinc is known for its essential role in the growth and mineralization of bone tissue. Previous research has suggested that zinc may promote osteoblast and chondrocyte differentiation and activity, while, at the same time, inhibiting osteoclast metabolism [13,14]. On the other hand, the effect of lithium on bone metabolism is unclear. Several studies revealed an inhibited effect of lithium on bone resorption and osteoclast formation while other studies found conflicting results [15-17]. Therefore, the underlying mechanism of the favorable osteogenesis property of Zn-Li alloy implants is still unknown. In this study, in vitro and in vivo experiments were combined to investigate the osteogenic activity and the biological mechanism of Zn-Li alloys. More importantly, a rabbit shaft fracture model was established to verify the feasibility of using Zn-Li alloy implants at high load-bearing sites.

#### 2. Materials and methods

# 2.1. Materials preparation

Pure Zn and Zn-Li alloys were prepared from Zn (99.99%) and Zn-Li master alloy (6 wt% Li) ingot by Hunan rare earth metal material research institute. Cast iron mold with ZnO coating was used for casting. The chemical compositions of pure Zn and Zn-Li alloys are listed in Table S1. The raw materials were homogenized at 350 °C for 48 h followed by water quenching. Then, the as-cast materials were deformed by hot extrusion at 260 °C with an extrusion ratio of 36:1 at 1 mm/s. Samples were prepared in two directions. One ( $\Phi 10 \times 1$  mm) was cut perpendicular to the extrusion direction (ED) while the other (10 imes 10 × 1 mm) was cut parallel to the extrusion direction (transverse direction, TD). For the microstructure observation, samples with both directions were used. For the rest of the in vitro tests, ED samples were used. All the samples were grounded to 2000 grit with SiC, followed by ultrasonically cleaning in acetone, absolute ethanol, and distilled water. For the rat femur model, rods ( $\Phi 1.6 \times 15$  mm) were machined from the as-extruded samples and grounded to 2000 grit and ultrasonically cleaned. Rods were sterilized by ethylene oxide before implantation. For the rabbit femoral shaft fracture model, bone plates and screws were fabricated from as-extruded Zn-0.4Li alloy and Ti-6Al-4 V alloy by Reach Medical Co., Ltd., Shanghai, China.

#### 2.2. Microstructure analysis

ED and TD samples were further grounded to 7000 grit and polished with a water-soluble 0.25  $\mu$ m diamond slurry on microfiber. Then the polished samples were chemical-etched with a 4% HNO<sub>3</sub>/alcohol solution for 5–10 s and visualized under scanning electron microscopy (SEM,

Hitachi S-4800, Japan). Thin foil samples (ED) for scanning transmission electron microscopy (STEM, FEI Titan  $G^2$  60–300 ChemiSTEM) observation were prepared by mechanically polishing to a thickness of 60–70 μm, followed by punching into 3 mm diameter disks, and ion-beam milling using Gatan PIPS 691 with 10 KeV at  $-25\,^{\circ}\text{C}$  to  $-30\,^{\circ}\text{C}$ . Samples were plasma cleaning by Gatan SOLARUS 950 before visualized under the high-resolution high-angle annular dark-field mode (HAADF) and selected area electron diffraction (SAED) at 300 kV. Samples (ED) for electron backscattered diffraction (FEI Nova 400 SEM equipped with HKL-EBSD system) mapping were mechanically grounded, followed by electron-chemical polishing in 5% HClO4 electrolyte. X-ray diffractometer (XRD, Rigaku DMAX 2400, Japan) using CuKα was operated at 40 kV and 100 mA with scanning range from  $15^{\circ}\text{-}70^{\circ}$  at a scan rate of  $2^{\circ}\text{-}min^{-1}$  and step of  $0.02^{\circ}$ .

#### 2.3. Mechanical tests

Samples for tensile tests were machined along the extruded rod according to ASTM-E08-04a and examined in a universal material test machine (Instron 5969, USA) at a displacement rate of  $1\times10^{-4}~\rm s^{-1}$ . The yield strength was determined as the stress at which the 0.2% plastic deformation occurred. Microhardness was carried out in a microhardness tester (SHIMADZUHMV-2 t) measuring Vickers hardness with 0.1 kN loading force and 15 s dwell time. An average of five measurements was taken for each group on the ED samples.

#### 2.4. Cytological study

#### 2.4.1. Cell culture and material extracts preparation

The mouse osteogenic precursor cell line MC3T3-E1 was used here to examine the cytocompatibility and osteogenic activity of samples. Cells were cultured in the  $\alpha\text{-MEM}$  (supplemented with 10% FBS, 1% penicillin ( $100~\text{U}\cdot\text{mL}^{-1}$ ), and streptomycin sulfate ( $100~\text{mg}\cdot\text{mL}^{-1}$ ), Gibco, Grand Island, NY) medium at 37 °C, 5% CO<sub>2</sub>, and saturated humidity. The extracts were prepared according to ISO 10993–5. Samples were immersed in the  $\alpha\text{-MEM}$  cell culture medium at a volume to area ratio of 1.25 mL cm $^{-2}$ . The extracts were incubated at 37 °C, 5% CO<sub>2</sub> for 24 h before collection and filtration, and then stored at 4 °C before use. The ion concentration in the extracts was detected by Inductively coupled plasma optical emission spectroscopy (ICP-OES, iCAP6300, Thermo Scientific, USA).

#### 2.4.2. Cell cytotoxicity evaluation

The Cell Counting Kit-8 (CCK-8, Dojindo Molecular Technology, Japan) was used to assess the proliferation activity of MC3T3-E1 cells. Cells were digested with 0.25% trypsin and centrifuged at 1200 rpm for 4 min when reaching 90% confluency. Then, 100  $\mu L$  cells were seeded in each well of a 96-well plate at a density of  $2\times10^4$  cells mL $^{-1}$ . Cells were incubated for 2–4 h with  $\alpha$ -MEM for attachment followed by replacement of sample extracts (supplemented with 10% FBS, 1% penicillin (100 U·mL $^{-1}$ ), and streptomycin sulfate (100 mg·mL $^{-1}$ ), Gibco, Grand Island, NY). Extracts with 1-fold dilution were used to test the cytocompatibility of samples at 24 h and 72 h co-culture with cells, with blank culture medium as control. The optical density (OD value) was then measured by using a microplate reader (Bio-Rad 680) at 450 nm. At least five measurements were taken in each group.

#### 2.4.3. ALP activity and staining

The MC3T3-E1 cells were seeded in a 6-well plate with 2 mL per well at a density of  $3\times 10^4$  cells  $mL^{-1}.$  Cells were incubated with culture medium to reach 80% confluency. Then the medium was replaced with an osteogenic induction solution prepared from the diluted sample extracts. The culture solution was refreshed every other day. After 7 and 14 days of differentiation, the cells were washed three times with PBS, and the ALP activity was assessed according to the ALP quantitative analysis kit protocol (Nanjing Jiancheng Bioengineering Institute,

China). Each group was tested in triplicates. At 14 days, cells cultured with 1-fold diluted extracts were stained using the ALP staining kit (Shanghai Hongqiao Chemical Reagent Inc., Shanghai, China) and observed under an optical microscope.

#### 2.4.4. Cell morphology

The MC3T3-E1 cells were cultured with one-fold diluted extracts for 72 h. Then cells were stained with Live/Dead viability kit and cytoskeletal staining (cytoskeleton labeled with phalloidin, nuclei stained with DAPI). The cell morphology was observed under a confocal laser scanning microscope (CLSM, Leica TCS SP2; Leica Microsystems, Heidelberg, Germany).

# 2.5. Data independent acquisition mass spectrometry (DIA-MS) quantitative proteomics

#### 2.5.1. Cell culture

MC3T3-E1 cells were seeded into 6-well plates at a concentration of  $1\times10^5~mL^{-1}$  and cultured in  $\alpha\text{-MEM}$  medium supplemented with 10% FBS, 100  $\,\text{U}\cdot\text{mL}^{-1}\,$  penicillin, and 100  $\,\mu\text{g}\cdot\text{mL}^{-1}\,$  streptomycin (Gibco, Grand Island, NY). After 24 h, the medium was replaced with one-fold diluted Zn-0.4Li alloy extracts with a fresh  $\alpha\text{-MEM}$  medium as control. After another 48 h cultivation, cells were washed three times with ice-cold PBS, detached using a cell scraper, and stored at  $-80~^{\circ}\text{C}.$ 

#### 2.5.2. Sample preparation for mass spectrometry (MS)

The samples were thawed out and resuspended in RIPA buffer. After sonication, samples were incubated at 80  $^{\circ}\text{C}$  for 10 min and then centrifuged at 1.4  $\times$  10 $^4$  g for 10 min at 4  $^{\circ}\text{C}$ . The supernatant was collected, and the protein concentration was measured through BCA protein assay according to the instruction.

According to the measured concentration, 50  $\mu g$  protein was taken from each sample and diluted to the same concentration and volume with urea lysate. 1.25 M DTT was added to the above protein solution and incubated at 55 °C for 30 min after fully mixing. Iodoacetamide was added to alkylate and placed at room temperature in dark for 15 min. Three times the volume of HEPES solution was added, achieving the final concentration of each component in the solution (2 M urea, 20 mM HEPES, pH 8.0). Trypsin-TPCK at a concentration of 1 mg mL $^{-1}$  was added and the samples were digested overnight at 37°C. Finally, the hydrolysis enzymatic reaction was stopped by adding phosphoric acid to adjust the pH to 3 and the samples were desalted on C18 reverse phase columns. After dried under vacuum, samples resuspended and iRT peptides (1:10) were added.

# 2.5.3. Liquid chromatography-tandem mass spectrometry (LC-MS/MS) measurement

Samples were measured on a Q Exactive HF-X mass spectrometer (Thermo Fisher, Bremen, Germany). A nano trap column was used ( $\Phi300~\mu m \times 5$  mm, packed with Acclaim PepMap100 C18, 5  $\mu m$ , 100 Å) before separation by reversed-phase chromatography (Acquity UPLC M–Class HSS T3 Column,  $\Phi75~\mu m \times 250$  mm) at 40 °C. Peptides were separated using an acetonitrile (ACN) gradient (in 0.1% formic acid) from 3% to 40% over 45 min at a flow rate of 250 nL·minute $^{-1}$ .

The Hyper Reaction Monitoring (HRM) Data Independent Acquisition (DIA) method included a resolution of  $1.2\times10^5$  (FWHM), scan range of 300–1500  $m\cdot z^{-1}$ , Automatic Gain Control (AGC) target of  $3\times10^6$ , and maximum injection time of 120 ms. Fragmentation was performed via Higher-Energy Collisional Dissociation (HCD) and precursor peptides were isolated at  $3\times10^4$  resolution from 300 to 1500 m·z $^{-1}$ .

## 2.5.4. Spectronaut analysis and data processing

The date of MS measurement was matched with the theoretical spectra in FASTA library, and signals were converted into peptide and protein sequence information. Then the spectral library was established by combining the sequence information, retention time of peptides, and

information of fragment ions. The raw DIA data of MC3T3-E1 cell groups were processed by Spectronaut 10 software to identify the significantly changed proteins. Metacore  $^{\text{TM}}$  (Thomson Reuters Inc.) was used to map significantly changing proteins onto biological pathways. The top 20 biological pathways were selected.

# 2.5.5. Parallel reaction monitoring (PRM) quantitative results of target proteins

Among the significantly changed proteins which showed in LC-MS/MS measurement, interesting proteins that may be related to osteogenesis were selected for further PRM verification. The list of target proteins was imported into SpectroDive software and the samples of the different groups were pre-scanned to complete the calibration. Then, the data of pre-scan was imported into the Xcalibur-PRM method mode of Q Exactive HF-X mass spectrometer, and the main scanning parameters were set, including the resolution of  $1.75 \times 10^4$ , the isolation window of  $1.2 \, \mathrm{m} \cdot \mathrm{z}^{-1}$ , the AGC of  $1 \times 10^5$ , maximum injection time of 200 ms, and HCD of 28.

#### 2.6. Rat femur model

#### 2.6.1. Surgical procedures

Rods ( $\Phi$ 1.6  $\times$  15 mm) of pure Zn and Zn-0.4Li alloys were implanted into the rat femur under sterile conditions. The detailed surgical procedure was described in our previous study. Briefly, rats were anesthetized by intraperitoneal injection of ketamine (10 mg·kg<sup>-1</sup>) and 2% xylazine (5 mg·kg<sup>-1</sup>). Each rat was immobilized and the right hind limb was shaved and depilated. A 15 mm long incision was made along the lateral side of the humerus to dislocate the knee joint. A cylindrical hole (1.6 mm in diameter) was drilled in the center of the femoral condyle and the rod was inserted into the right femur. The wound was closed carefully. Each rat was implanted with one rod. At least six implants of each material were used. At least twelves male Sprague Dawley rats aged 3 months and weighted by an average of 200 g were randomized to each group. After 8 weeks, the rats were sacrificed and the right femurs were explanted and fixed in 10% neutral formalin buffer. X-ray, Micro-CT, and histological analysis were performed afterward. All the animal procedures have complied with relevant ethical regulations for animal research and were approved by the Animal Ethical Committee at the Ninth People's Hospital affiliated to Shanghai Jiaotong University, School of Medicine (Shanghai, China).

#### 2.6.2. Micro-CT analysis

The explanted rat femur was visualized under a Micro-CT system (Skyscan 1172 Bruker Micro-CT N.V., Kontich, Belgium). A 20  $\mu m$  protocol (100 kV, Al + Cu filter,  $0.6^{\circ}$  rotation step, frame averaging of  $2^{\circ}$ ,  $360^{\circ}$  rotation) was adopted for the scanning. The degradation rate (DR) was calculated based on the following equation:

$$DR = \frac{V_0 - V_t}{At}$$

Where  $V_0$  is the volume of the implant before implantation,  $V_t$  is the volume of the implant at the designated time interval, t is the implantation time, and A is the initial implant surface area.

# 2.6.3. Histological analysis

The implants were rinsed in water, dehydrated in ethanol, cleared in xylene, and embedded in methyl methacrylate. The sections were cut perpendicular to the long axis of the implant in the femoral condyle. Sections were ground, polished, and stained with van Gieson's Picrofuschin. The samples were visualized under a high-quality microscope (Olympus CKX41, Japan). Bone-to-implant contact (BIC) and bone area (BA) were quantitively measured according to the same method reported before.

#### 2.6.4. Cross-sectional analysis

The embedded sample was further cut into a 1 mm-thickness slice. The slice was grounded to 7000 grit and polished with a water-soluble 0.25  $\mu m$  diamond slurry on microfiber. The finalized slices were coated with a thin layer of gold and visualized by SEM equipped with EDS (SEM, Hitachi S-4800, Japan).

#### 2.7. Rabbit shaft fracture model

A rabbit shaft fracture model was established to evaluate the load-bearing capability of Zn-0.4Li alloy with Ti-6Al-4 V as control. Female

New Zealand rabbits weighed around 2.5 kg were selected and the alloys were fabricated as orthopedic fixation (plates and screws) from the asextruded samples by Reach Medical Co., Ltd. After making a fracture in the middle part of the femur, internal fixation was carried out to ensure the fracture was properly fixed. X-ray test was performed at a predetermined time point (post-surgery, 3 months, and 6 months) to observe the fracture healing. Rabbits were sacrificed at 6 months and femurs containing internal fixation devices were collected for Micro-CT visualization (Scanco Micro-CT100, 18  $\mu m$ , 66 Kv, 110  $\mu A$ ). Undecalcified samples containing implants were fixed by 4% formaldehyde buffer and dehydrated through ethanol of different concentrations. Then, the

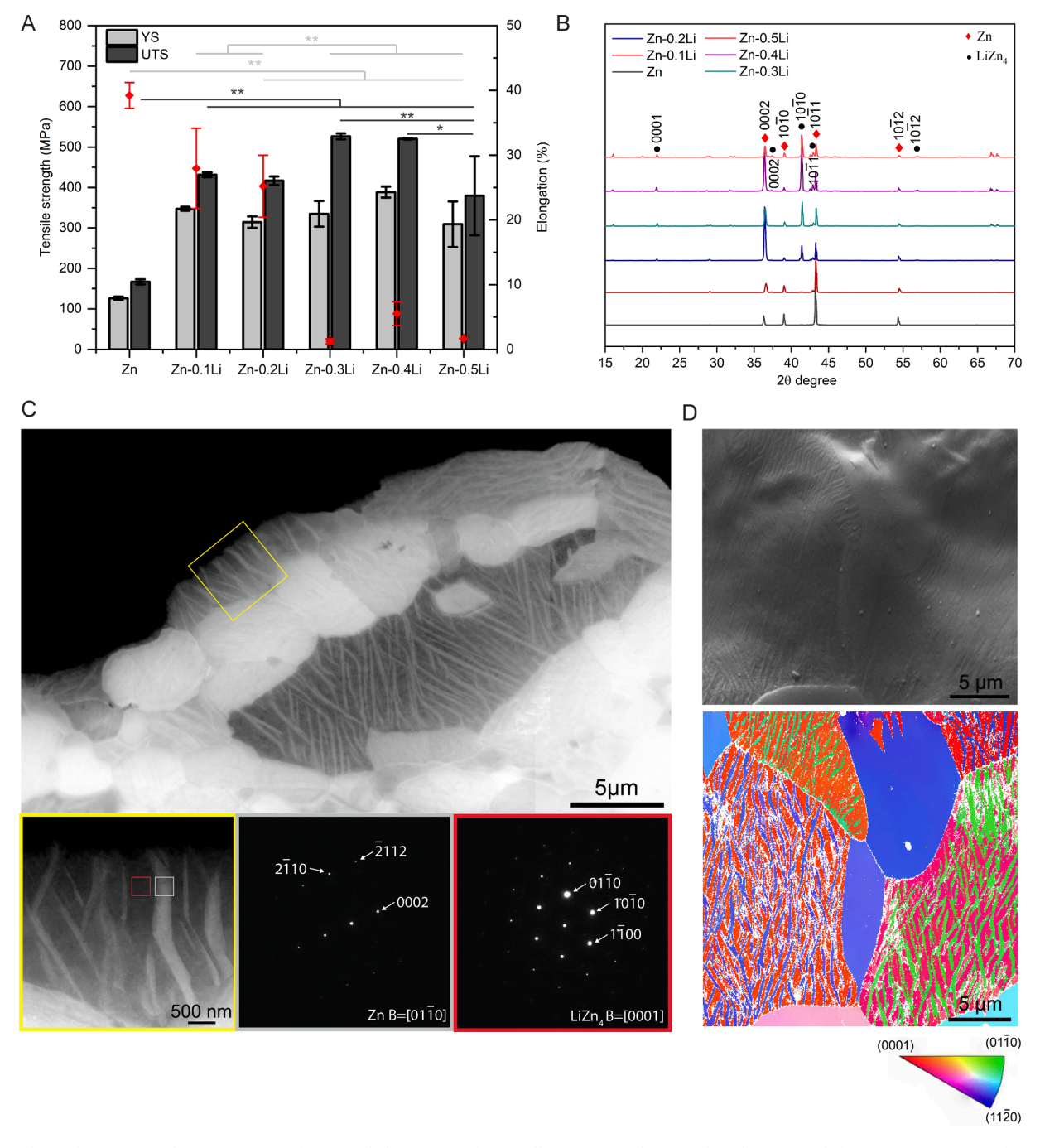


Fig. 1. Mechanical property and microstructure of as-extruded pure Zn and Zn-Li alloys. (A) Tensile strength and (B) X-ray diffraction patterns. Error bars indicate mean  $\pm$  standard deviation (n = 3). (C) HADDF-STEM image and SAED patterns of the Zn-0.4Li alloy. The magnification is marked by the yellow square. SAED patterns correspond to areas marked by red and grey squares in the magnification, respectively. The pattern of Zn and LiZn<sub>4</sub> are indexed with zone axis  $[01\overline{1}0]$  and [0001], respectively. (D) Inverse pole figure (IPF) maps of the Zn-0.4Li alloy. \*p < 0.05, \*\*p < 0.01, black lines and asterisks represent ultimate tensile strength, light gray lines and asterisks represent elongation.

samples were soaked in methyl methacrylate (MMA). After several months, the samples were longitudinally cut with a thickness of approximately 50  $\mu$ m. Finally, slides were stained with Van Gieson and Paragon and observed under a microscope.

#### 2.8. Data analysis

Data analysis was performed using SPSS 18.0 statistical software (SPSS Inc. Chicago, USA). Quantitative data are expressed as mean  $\pm$  standard deviation (SD). Data were analyzed using the t-test for independent samples, one-way analysis of variance (ANOVA), and Tukey's multiple comparison test. Differences were considered statistically significant at p<0.05 or p<0.01.

#### 3. Results

#### 3.1. Mechanical property and microstructure

Fig. 1A and Fig. S1 reveal that Li demonstrated a significant strengthening and hardening effect in Zn, whereas the ductility reduced significantly with Li contents. Among them, Zn-0.4Li alloy exhibited optimal mechanical performance. XRD diffraction patterns (Fig. 1B) show that Zn and LiZn<sub>4</sub> were the major phases in Zn-Li alloys, and their peaks became stronger with Li contents. According to the Zn-Li binary phase diagram [18],  $\beta$ -LiZn<sub>4</sub> decomposed into Zn and  $\alpha$ -LiZn<sub>4</sub> at 65 °C in the thermodynamic equilibrium condition. The rods were air-cooled after hot extrusion (260°C), thus  $\alpha$ -LiZn<sub>4</sub> could be the dominant intermetallic phase. Two regions were identified based on the bright and dark contrast in SEM images (Fig. S2A and B). The standard electrode potential of Li (-3.04 V) is much lower than that of Zn (-0.76 V). Therefore, the LiZn<sub>4</sub> phase is more vulnerable to corrosion during etching. The brighter regions with higher corrosion resistance should be Zn (white

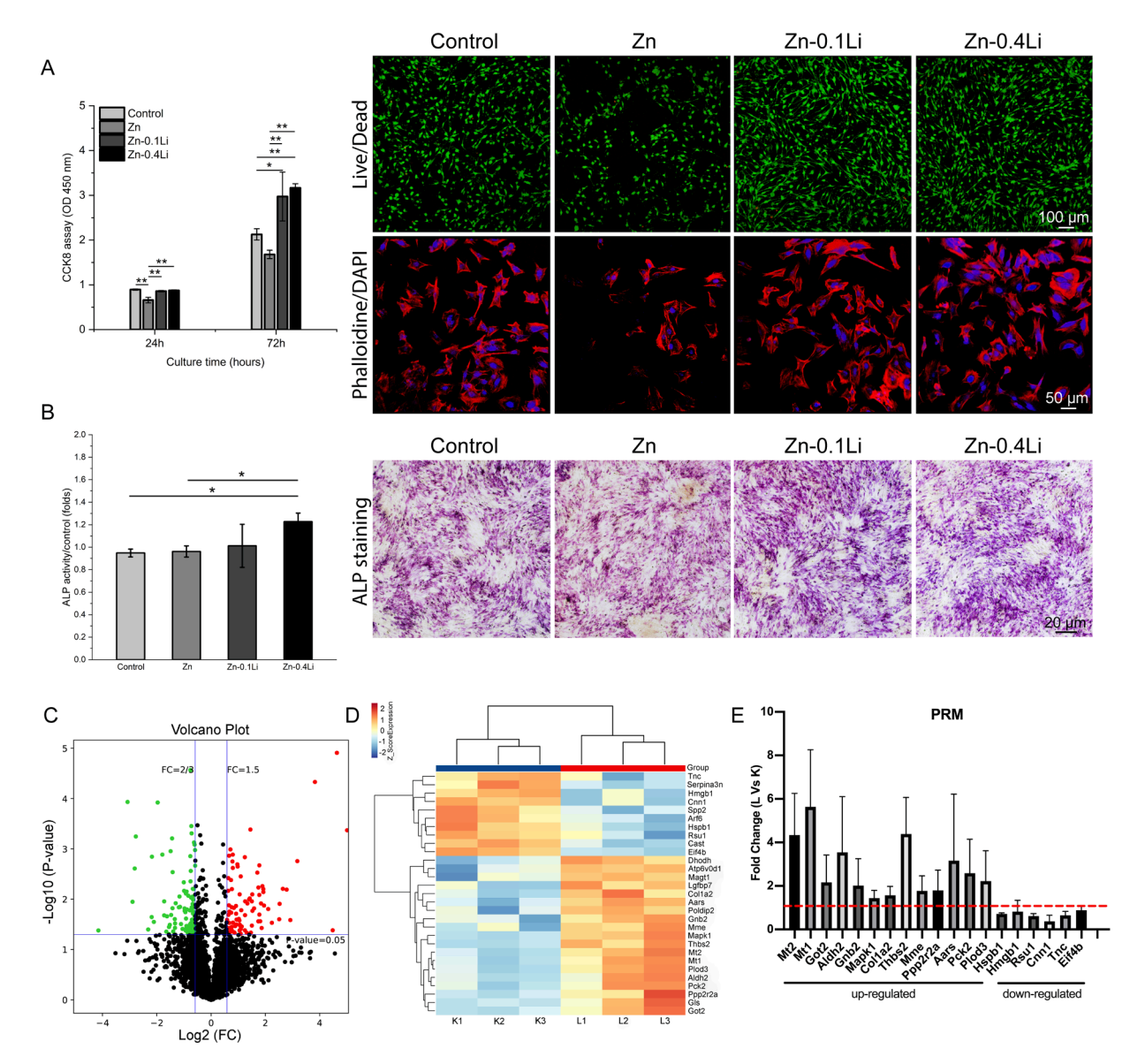


Fig. 2. Cell viability, osteogenic differentiation activity, and DIA-MS quantitative proteomics of MC3T3-E1 cells after co-culture with one-fold diluted pure Zn and Zn-Li alloy extracts. (A) Cell viability (n = 6), live/dead staining, and cytoskeletal staining. (B) ALP activity and staining of cells after 14 days' culture with materials extracts (n = 6). (C) Volcano plot displaying down- (green) and up- (red) regulated proteins by Log10 p-value and Log2 fold change (FC $\geq$ 1.5 or  $\leq$ 2/3 and p-value < 0.05). (D) A heat map showing the 30 regulated proteins (K: control group, L: Zn-0.4Li alloy group). (E) PRM results of selected proteins (n = 3, up regulated: 13, down regulated: 6). \*p < 0.05, \*\*p < 0.05. Error bars indicate mean  $\pm$  standard deviation.

arrows). In contrast, the darker regions with more severe etching feature should be the eutectoid phase (Zn + LiZn4) (red arrows). The area fraction of the darker region increased with higher Li contents. The magnifications revealed a lamellar structure in the eutectic phase, which arranged along the extrusion direction.

To further look into the strengthening effect of Li on the Zn matrix, STEM, SAED and EBSD were performed on Zn-0.4Li alloy. HADDF image (Fig. 1C) found two phases with apparently different structures. One was in a brighter feature while the other was in a darker feature with lamellar structure. The intensity in the HADDF image is proportional to the square of the atomic number. Therefore, Zn should be the brighter phase with a size of about several microns while the relatively darker phase with lamellar structure is the eutectoid phase  $(Zn + LiZn_4)$ . Inside the eutectoid phase (yellow square), the needle-like precipitates (grey square) were the Zn generated by eutectoid decomposition. The rest of the dark regions were LiZn<sub>4</sub> (red square). The lamellar structure, in the width of approximately 300 nm, is an effective structure to strengthen the Zn matrix. SAED and EBSD (Fig. 1C, D) identified two orientations in the lamellar structure. The c-axis of Zn (blue or green regions in the IPF) was perpendicular to the extrusion direction, which was the same as adjacent Zn grains. In contrast, the c-axis of LiZn<sub>4</sub> (red regions in the IPF) was parallel to the extrusion direction. For the following sections, Zn-0.1Li and Zn-0.4Li alloys were selected as representative groups considering their contents and mechanical performance, with pure Zn as

#### 3.2. Cytological evaluation

Fig. 2A depicts the cell viability and morphology of MC3T3-E1 cells after culture with one-fold diluted extracts. Pure Zn showed an inhibited effect on the cell viability for both 24 h and 72 h compared to the control group. In contrast, Zn-Li alloy groups exhibited similar value to that of the control group in 24 h while significantly improved cell proliferation was found in 72 h. Live and dead staining further confirmed the results of cell viability. In cytoskeletal staining, cells showed healthier and more spread morphology in Zn-Li alloy groups than that of the pure Zn group. The osteogenic activity of MC3T3-E1 cells after 14 days' culture with extracts is presented in Fig. 2B. Zn-0.4Li alloy group showed significantly higher ALP activity than that of pure Zn and control groups. The ALP staining was consistent with the quantitative results. The concentrations of  $\text{Zn}^{2+}$  and  $\text{Li}^{1+}$  ions in the 100% extracts are presented in Table S2. Compared to pure Zn, alloying with Li decreased the release of Zn<sup>2+</sup> ion during degradation. The concentration of Li<sup>1+</sup> ion was up to 2.38 µg/ml in the Zn-0.4Li alloy extract.

Considering the optimal performance of Zn-0.4Li alloy on the viability and differentiation of osteoblasts, DIA-MS quantitative proteomics was conducted to look into the proteome modulation by Zn-0.4Li alloy extracts. In both the protein interaction diagram and the bubble chart (Fig. S3), we found that the Zn-0.4Li alloy group showed significant effects on some signaling pathways. Among them, the PI3K-AKT and ECM receptor signaling pathways may play an important role in osteogenesis differentiation. In the volcano plot (Fig. 2C), 194 significantly regulated proteins were determined with criteria including FC $\geq$ 1.5 or  $\leq$ 2/3 and p-value < 0.05. Among them, 109 down-regulated proteins were expressed in green dots while 86 up-regulated proteins were showed in red dots. The larger the distance between dots and zeropoint means the greater the significance. In the Heat Map (Fig. 2D), we listed 30 target proteins selected from 194 significantly changed proteins, which may highly related to osteogenic differentiation according to previous studies [19-26]. For example, Thbs2 has been reported to promote mineralization by facilitating the proper organization of the osteoblast-derived ECM [26]. The dysfunction of Col1a2 affects collagen quantity or structure, which leads to osteogenesis imperfecta [21]. Aldh2 promotes osteoblast differentiation via bone morphogenetic protein-2 and induces bone anabolic effect [20]. The downregulation of CNN1 promotes the expression of BMP2-Smad signal [27], etc. Red

represents high-expressed proteins and blue represents low-expressed proteins. It was found that the Zn-0.4Li alloy treated group (L1-3) showed significant changes in protein expression compared with the control group (K1-3), including several genes closely related to osteogenic differentiation, such as MAPK1 (ERK), Col1a2, Mt1, and Mt2. Fig. 2E shows the quantitative PRM results of the target proteins, which verified the significantly different expression of 19 proteins. Note that 13 proteins were significantly up-regulated (Mt2, Mt1, Got2, Aldh2, Gnb2, Mapk1, Col1a2, Thbs2, Mme, Ppp2r2a, Aars, Pck2 and Plod3) while 6 proteins were down-regulated (Hspb1, Hmgb1, Rsu1, Cnn1, Tnc and Eif4b).

#### 3.3. Osteogenic evaluation and degradation analysis

A rat femur model was used here to study the osteogenic activity and degradation behavior of Zn-0.4Li alloy, with pure Zn as control. The Xray images showed an excellent radiopacity of the Zn based implants (Fig. 3A). No osteolysis, deformation, dislocation, or gas shadow were found in the implantation sites. The adjacent cortical bone showed higher radiographic density over time, indicating the circumferential osteogenesis. The reason that the Zn implant post-surgery was not ideally aligned to the long axis of femur maybe due to the different postures during X-ray photograph or human factors. Compared to pure Zn, more new bone tissue was observed surrounding the Zn-0.4Li implant in the 3D reconstruction image (Fig. 3B). Both implants maintained the integrity after 8 weeks' implantation. The degradation rates for them were 0.15 mm/year approximately without significant difference (Fig. 3C). Van Gieson staining found new bone tissue around both implants at week 8 (Fig. 3D). For pure Zn, newly formed bone distributed sparsely around the implant. In contrast, larger amounts of new bone were visible surrounding the Zn-0.4Li implant. MASSON staining indicated that more collagen was formed in the Zn-0.4Li alloy group with a more mature state than that of the pure Zn group. The quantitative analysis confirmed a significantly higher new bone area (BA) in the Zn-0.4Li alloy than that of pure Zn (Fig. 3E). As for osteointegration, localized bone bonding with implants was found in both implants, but intervening fibrous tissue occupied most of the area. To analyze the degradation of implants, the representative cross-sectional images with elemental mapping are displayed in Fig. 3F. Based on the mapping, three distinct parts were visible in both implants. The Zn based matrix was highlighted by red. New bone was rich in Ca and P with tissue that marked in green. Degradation products in pure Zn were found in the bone-implant interface, mainly consisting of Zn and O. In contrast, only small amounts of them were visible in Zn-Li alloy.

### 3.4. Load-bearing capability and bone fracture healing

To evaluate the biodegradable Zn-Li alloy as load-bearing bone implants, we established a rabbit shaft fracture model, with Ti-6Al-4 V alloy as control. Good alignment of fracture ends was shown by X-ray images post-surgery. Progressive healing was observed for both implants over time (Fig. 4A). The fracture line became blurred at month 3 and was replaced by cortical bone bridging at the fracture site after 6 months. Callus formation was recorded in both groups. Zn-0.4Li alloy group showed a bigger callus tissue area than that of the Ti-6Al-4 V alloy group. Micro-CT further confirmed that the bone fracture healed completely and the fracture line disappeared after 6 months (Fig. 4B). Both groups remodeled towards normal bone matrix and geometry. Von Gieson staining and Paragon staining are performed to study the tissue response during fracture healing (Fig. 4C). At month 6, new cortical bone formed at the fracture site in both groups. Compared to the Ti-6Al-4 V alloy group, the cortical bone in the Zn-0.4Li alloy group was much thicker, showing similar thickness to the proximal and distal normal cortical bone. Also, new bone formed around the screw thread, showing good osteointegration in both groups. Furthermore, new bone grew into the screw hole, even covering the screw head, showing good bone

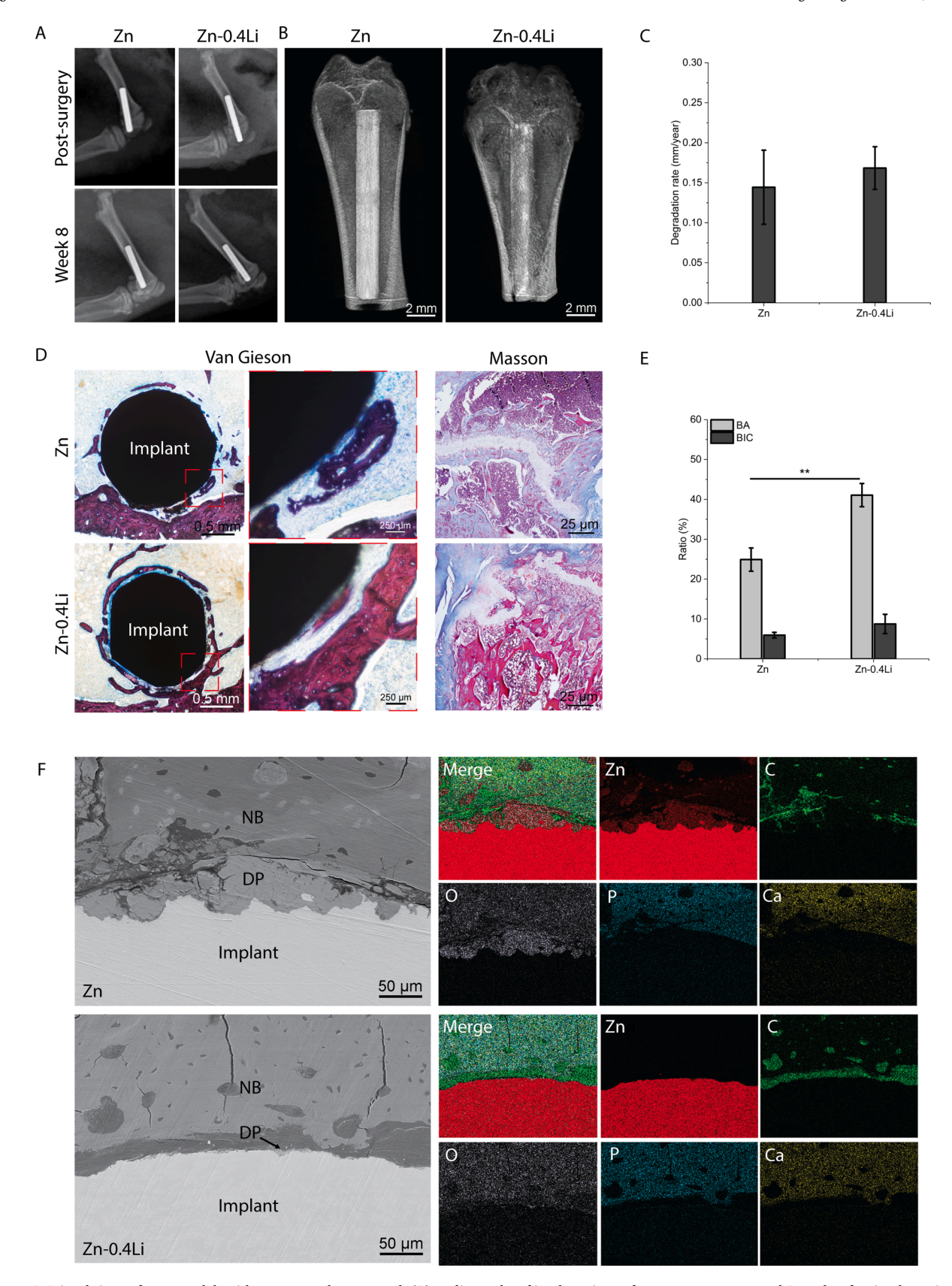


**Fig. 3.** Zn-0.4Li rods in rat femur model, with pure Zn rods as control. (A) Radiographs of implants in rat femurs post-surgery and 8 weeks after implantation, (B) 3D Micro-CT reconstruction after 8 weeks implantation, (C) degradation rate based on volume loss (n = 4), (D) Van Gieson and Masson staining of representative cross sections in week 8, the magnifications are marked by red rectangle, (E) bone area (BA) and bone-implant contact ratio (BIC) (n = 4), (F) SEM cross sectional image with corresponding elemental mapping. NB, new bone; DR, degradation products. \*p < 0.05, \*\*p < 0.01. Error bars indicate mean  $\pm$  standard deviation.

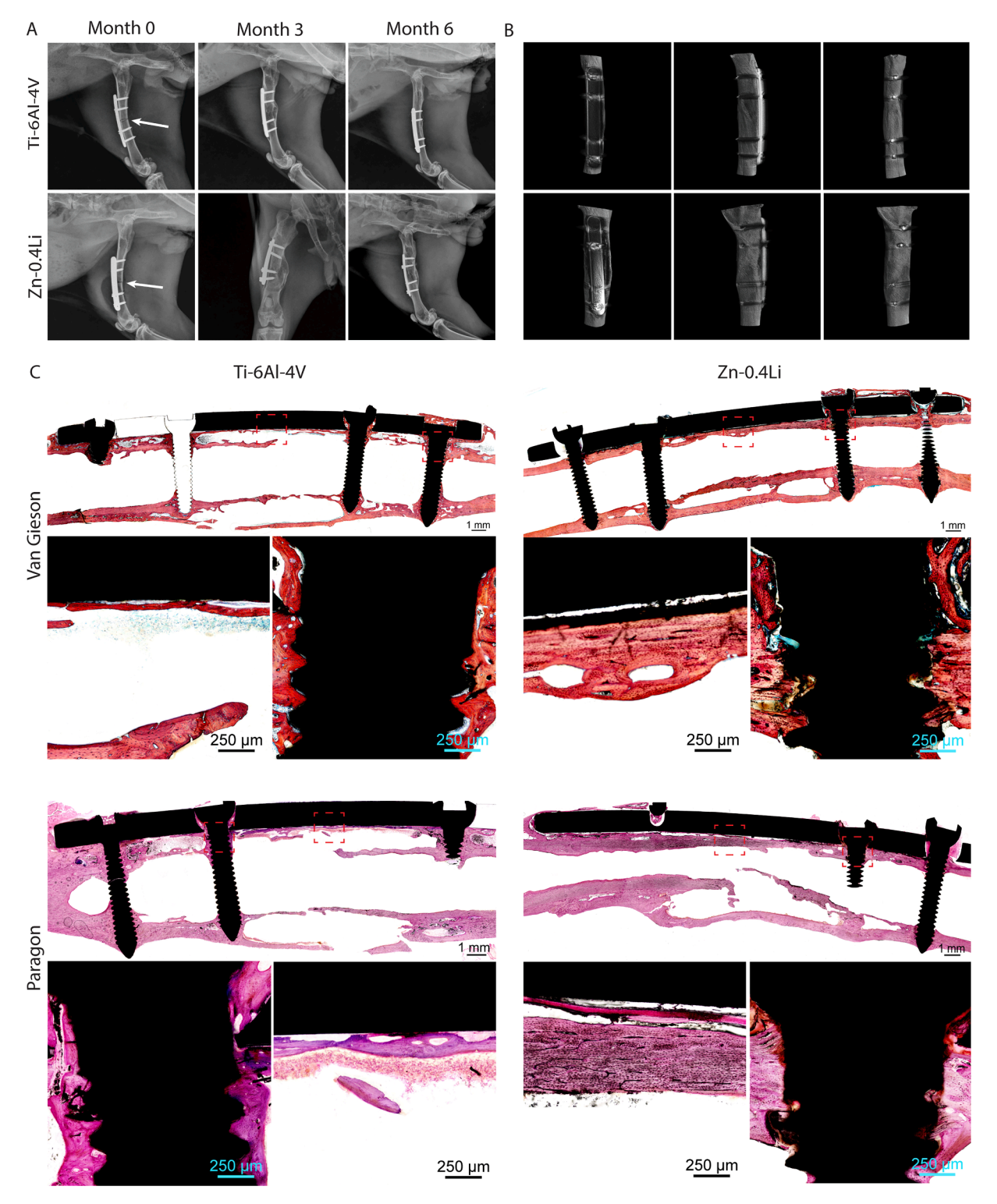


Fig. 4. Zn-0.4Li fixation plate and screw in rabbit femoral shaft fracture model, with Ti-6Al-4 V alloy plate and screw as control. (A) Representative X-ray images of rabbit femurs after 0, 3, and 6 months post-surgery, fracture line is indicated by write arrows, (B) Micro-CT reconstruction of rabbit femoral shaft with plate and screw system at 6 months, (C) Van Gieson staining and Paragon staining of representative histological images of femoral fracture healing at 6 months. The fracture healing and fixation screws are magnified and marked by red rectangles.

ingrowth capability. Paragon staining showed no obvious inflammatory reactions for both groups at month 6. It is worthy to note that more osteocytes presented in the new bone tissue in the Zn-0.4Li alloy group than that of the Ti-6Al-4 V alloy group. No sign of gas formation was found around Zn-0.4Li implants. Therefore, Zn-0.4Li alloy demonstrated a comparable and even better performance than Ti-6Al-4 V alloy in bone

fracture healing. The H&E staining of heart, kidney, liver, lung, and spleen showed no abnormalities or pathological morphologies in both groups (Fig. S4). Blood routine examination and serum biochemical tests presented no significant difference in both groups either (Table S3).

#### 4. Discussion

#### 4.1. Osteogenic mechanism of biodegradable Zn-Li alloys

In this study, Zn-0.4Li alloy was able to release Zn ions and Li ions simultaneously during the degradation (Table S2). Compared to pure Zn, Zn-0.4Li alloy significantly promoted the proliferation and ALP expression in MC3T3-E1 cells. More importantly, the rat femur model proved that the new bone volume around the Zn-0.4Li alloy implant was significantly increased compared to that of pure Zn implant (Fig. 3E). Therefore, it is reasonable to conjecture that the degradation products of Zn-0.4Li alloy exerted a better osteogenic ability than pure Zn. The osteogenic mechanism of Zn-0.4Li alloy was further explored by DIA-MS quantitative proteomics and parallel reaction monitoring (PRM). PRM verified that 19 proteins, which were closely related to osteogenesis, were significantly regulated by Zn-0.4Li alloy extracts.

The schematic diagram of the corresponding pathway, PI3K-AKT, which is a bone-repair related signaling pathway, is illustrated in Fig. 5. PI3K-AKT signaling pathway plays an important role in osteogenic differentiation, which has been proved to be the main mechanism in some natural compounds like microRNA and exosomes to promote bone repair [28]. The significantly up-regulated THBS and Col1a2 are the "starting point" in the PI3K-AKT signaling pathway, which firstly stimulates the membrane protein named FAK. Also, another elevated membrane protein Gnb2 works as a second way to activate the PI3K-AKT signaling pathway. Pck2 and ERK in the cytoplasm are the downstream proteins. Pck2 regulates glycolysis and gluconeogenesis while ERK has an impact on cell proliferation, angiogenesis, and DNA repair. In addition to stimulating the PI3K-AKT signaling pathway, we found that the expression of Zn binding protein metallothioneins (both MT1 and MT2), which involved in the intracellular Zn storage and bone formation [29], were elevated more than two-fold in the Zn-0.4Li alloy group (Fig. 2E). Futhermore, upregulated Col1a2 promotes the expression of type I collagen as well, which may promote the formation of new

bone directly [30]. Therefore, the Zn-0.4Li alloy could promote bone formation through various mechanisms, including the activation of the PI3K-AKT pathway and stimulation of metallothionein proteins.

# 4.2. The potential use of Zn-Li implants in high load-bearing applications

The load-bearing capacity and the tensile strength of the major clinically available non-degradable and degradable biomaterials for orthopedic implants are illustrated in Fig. 6. For decades, titanium (Ti) and its alloys, stainless steel, and cobalt-chromium (Co-Cr) alloys have been the primary implant materials used in high-load bearing sites such as long bone fractures, femur fractures, and joint replacements [1,31]. The common features of these materials include, but are not limited to. adequate mechanical strength and satisfactory biocompatibility. The tensile strength of these metallic materials is usually higher than 500 MPa, which can provide the injured bone tissue with sufficient mechanical support during bone healing [12]. Meanwhile, their biosafety is clinically acceptable. However, there are major known limitations for these inert metallic implants. First, the long-term implantation of inert metallic implants may induce unexpected clinical complications, such as chronic inflammation or pain, which may eventually lead to the removal of the implant via a second surgery [32]. Second, the high elastic modulus of metallic implants disturbs the original stress-strain trajectory in low-modulus bone tissue. This mismatch can lead to peri-implant bone loss over time (stress shielding), ultimately resulting in revision surgery [33].

Considering these limitations, the concept of "biodegradable implants" was proposed by clinicians and scientists [34]. Biodegradability means that the implants can pass through or be metabolized or assimilated by cells and/or tissue, and then dissolve completely upon fulling the mission to assist with tissue healing [35]. Therefore, the second surgery and stress shielding are no longer a concern since there will be no implant left.

Biodegradable polymers such as polyglycolide (PGA), polylactide

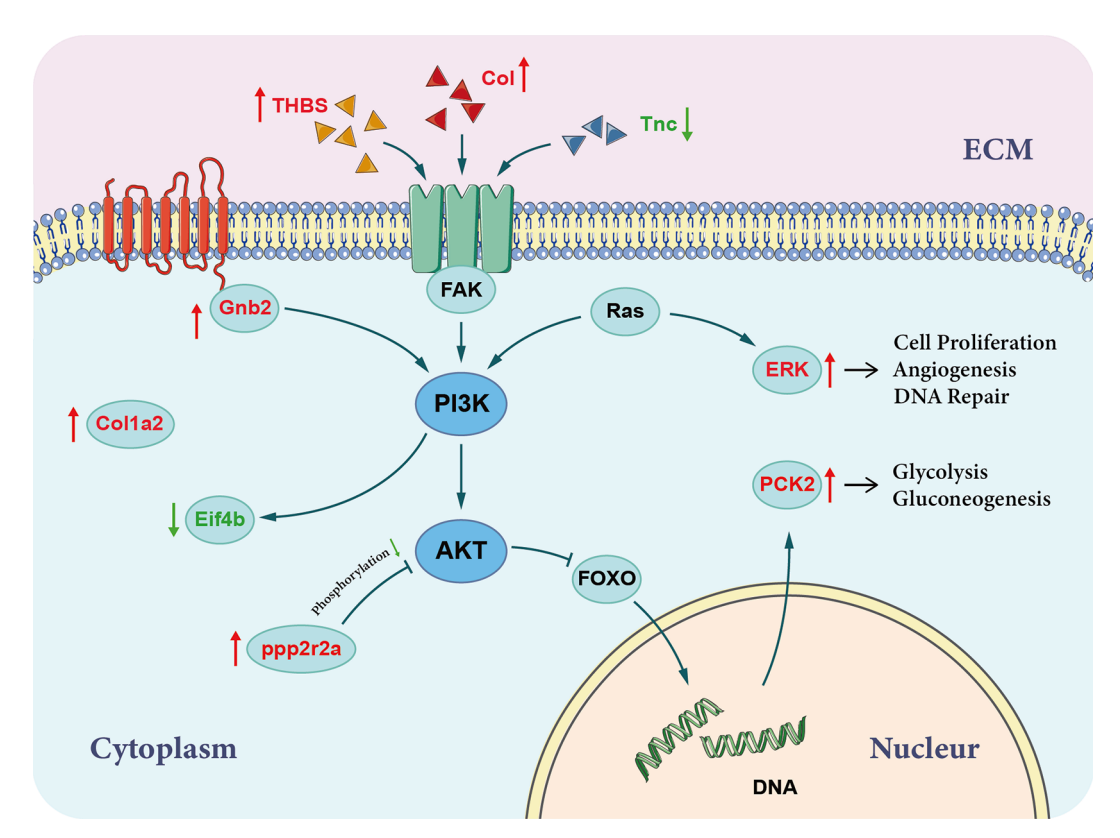


Fig. 5. The Schematic diagram of PI3K-AKT pathway. Red arrows indicate up-regulated proteins, while green arrows indicate down-regulated proteins.

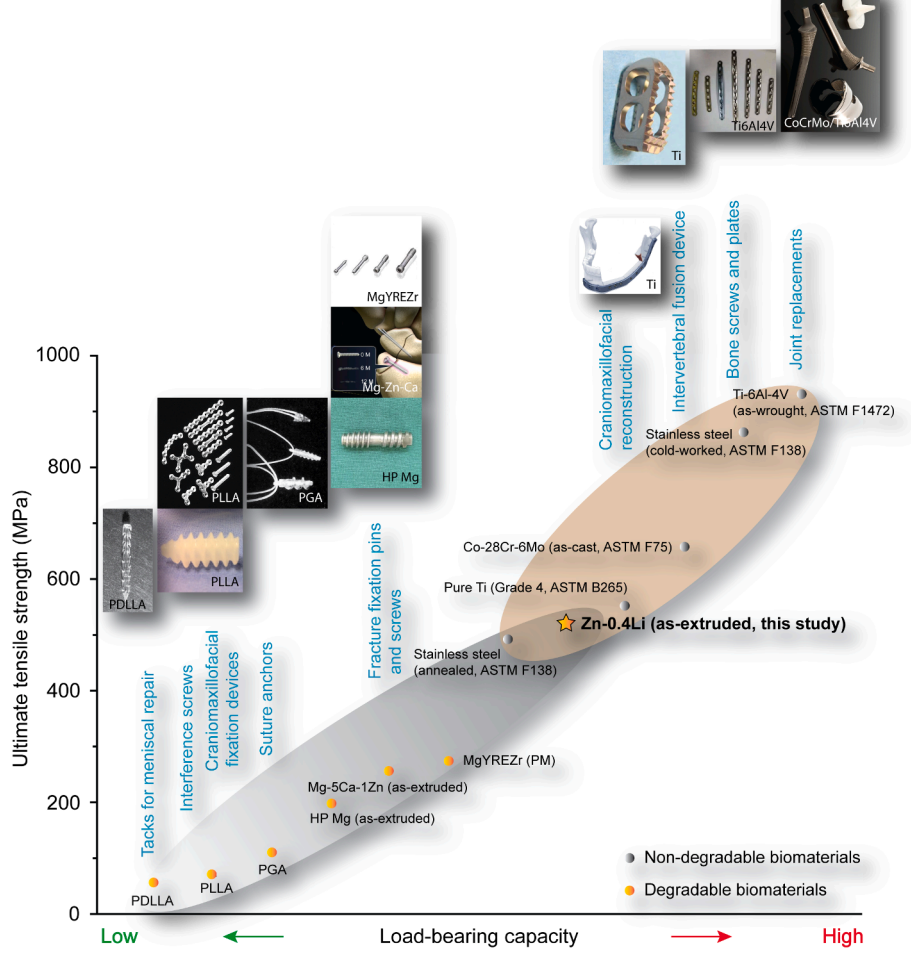


Fig. 6. The load-bearing capacity and tensile strength of clinically available non-degradable and degradable biomaterials for orthopedic implants.

(PLA), and poly (L- or D, L-lactic acid) (PLLA/PDLLA) have been widely used for many years as orthopedic fixation implants with FDA approval [6]. But their applications are limited at low load-bearing sites like nonload bearing bone fractures or soft tissue graft fixation due to their low strength [36]. Also, noninfectious inflammatory reactions may happen from time to time due to the acidic intermediate degradation products caused by the bulk erosion of polymers in physiological environments [7]. As an alternative, a burgeoning number of studies is dedicated by researchers to biodegradable metallic materials with better mechanical performance [34,37-39]. Among them, magnesium (Mg)-based implants have been transferred from scientific research to clinical applications after many years of development [8-10]. The in vivo degradation of Mg exerts beneficial effects on promoting bone regeneration and accelerating healing in bone diseases [8,40]. The bioactivity of Mg in the bone environment provides the Mg-based implants with a distinct advantage over other candidates for the treatment of challenging bone disorders. However, the strength of Mg-based metals is still far from the benchmark of inert counterparts, which limits their applications at high loadbearing sites.

Recently, Mg-based implants have been designed as supplements to high strength bioinert implants when treating fracture fixation [41]. For example, an innovative Mg/Ti hybrid fixation system was developed for long bone fracture fixation. Ti played the role of load bearing while Mg was responsible for promoting fracture healing via releasing Mg ions during degradation [42]. The rabbit tibia in the hybrid group showed better mechanical strength and faster endochondral ossification than the Ti control group [43]. However, the hybrid system may compromise the

initial idea of biodegradable implants. Besides, the unsatisfying degradation mode of Mg-based implants should be further optimized as the gaseous products may lead to cavities and inflammatory reactions. Therefore, no biodegradable implants have been applied to high load-bearing applications yet.

Recently, we found that the Zn-Li alloy system exhibited comparable high strength (UTS 431.27-520.36 MPa) to pure titanium as well as satisfying plasticity (elongation 5.51-27.96%) [12]. The lamellar structure of Zn and LiZn<sub>4</sub> played an effective role to strengthen the Zn matrix. Another study reported a combined high strength and high ductility in this structure [44]. Sub-micron grains and pinning effects caused by nano LiZn<sub>4</sub> precipitates also contribute to the high strength [45]. Therefore, we used a rabbit shaft fracture model in this study to further explore the feasibility of using devices made of Zn-Li alloys at high load-bearing sites. In general, the Zn-0.4Li alloy group displayed a similar fracture healing progress over the 6 months compared to the Ti-6Al-4 V alloy group. The bone fracture healed completely and the fracture line disappeared after 6 months. Both groups remodeled towards normal bone matrix and geometry. Interestingly, we found that the cortical bone at the fracture sites was much thicker in the Zn-0.4Li alloy group compared to the Ti-6Al-4 V alloy group. This can be explained by the beneficial role of Zn-0.4Li alloy in promoting new bone formation as discussed above. Besides, the Zn-0.4Li alloy group induced larger callus than the Ti-6Al-4 V alloy group at 3 months. This could be attributed to the capability of zinc to inhibit the osteoclast activities and bone resorption [46,47], but instable fixation due to screw degradation may contribute to the callus as well, further study is needed to look into this phenomenon. Therefore, Zn-0.4Li alloy was shown to combine the desirable aspect of bioinert metallic materials, namely adequate strength, with the bioactivity of Mg-based materials.

As for the degradation behavior, the implants should maintain the mechanical support for at least 12-24 weeks to allow sufficient healing of the fractured bone. However, a longer period is required to allow new bone tissue to fully mineralize and consolidate when treating long bone fractures like femur and tibia. Clinical data show that more than 20 months are needed for patients to bear external fixators [48]. The Zn-0.4Li alloy plates and screws retained mechanical integrity after 6 months' implantation, indicating the capability of long-term mechanical support for long bone healing. After assisting bone healing, the implants should degrade at an appropriate rate without causing serious inflammation or side effects. The recommended daily intake of element Zn is 12-15 mg for adults [49]. The daily release of Zn ion from the Zn-0.4Li implants was<0.24 mg if assuming the weight loss converts to Zn ion completely based on the Micro-CT results (Fig. 3C). Therefore, Zn-0.4Li alloy leaves sufficient room to tailor its degradation rate under the premise of biosafety.

To further move the application of biodegradable Zn-Li implants from bench to bedside, additional studies will be needed in the following topics: 1) the role of Li in the strengthening mechanism, degradation behavior, and biological response of Zn-Li alloys; 2) the impact of load on the degradation and failure of Zn-Li implants; 3) large animal models focus on the long-term fracture healing, implant degradation, and biosafety issues. It should be noted that the results presented here cannot be directly applied to what might happen in patients.

#### 5. Conclusion

In conclusion, we prepared Zn-Li alloys with comparable strength to that of commercially pure titanium. The alloy extracts promoted the proliferation and differentiation of MC3T3-E1 cells significantly compared to pure Zn. Results in the rat femur model confirmed a significantly better osteogenic activity of Zn-0.4Li alloy in contrast to that of pure Zn. DIA-MS quantitative proteomics found that the Zn-0.4Li alloy can promote bone formation through activation of the PI3K-AKT pathway and stimulation of metallothionein proteins. More importantly, the bone plates and screws made of Zn-0.4Li alloy exhibited a comparable performance in bone fracture fixation compared to the Ti-6Al-4 V counterpart. The fractured bone healed completely and remodeled towards normal bone matrix and geometry after 6 months post-surgery. The biodegradable Zn-Li alloy offers a promising option to fill the gap in biodegradable implants in high load-bearing applications.

#### 6. Data availability

All the data supporting the results of this study are available within the article and its supplementary information. Raw data are available from the corresponding authors upon request.

### **Declaration of Competing Interest**

The authors declare that they have no known competing financial interests or personal relationships that could have appeared to influence the work reported in this paper.

## Acknowledgements

The authors would like to thank Dr. Q. D. Zu (OE Biotech, Inc., Shanghai, China) for assistance with the bioinformatics analysis of Data-Independent Acquisition (DIA). This work was supported by the National Natural Science Foundation of China (Grant No. 51931001), the Shanghai "Rising Stars of Medical Talent" Youth Development Program (Youth Medical Talents - Specialist Program, Grant No. 201972).

#### Appendix A. Supplementary data

Supplementary data to this article can be found online at https://doi.org/10.1016/j.cej.2021.129317.

#### References

- [1] M. Geetha, A.K. Singh, R. Asokamani, A.K. Gogia, Ti based biomaterials, the ultimate choice for orthopaedic implants - A review, Prog. Mater. Sci. 54 (2009) 397–425, https://doi.org/10.1016/j.pmatsci.2008.06.004.
- [2] Y. Okazaki, E. Gotoh, Comparison of metal release from various metallic biomaterials in vitro, Biomaterials 26 (2005) 11–21, https://doi.org/10.1016/j. biomaterials.2004.02.005.
- [3] M. Ridzwan, S. Shuib, A. Hassan, A. Shokri, M.M. Ibrahim, Problem of stress shielding and improvement to the hip implant designs: A review, J. Med. Sci. 7 (2007) 460–467
- [4] J.R. Martin, C.D. Watts, D.L. Levy, R.H. Kim, Medial tibial stress shielding: a limitation of cobalt chromium tibial baseplates, J. Arthroplasty 32 (2017) 558–562, https://doi.org/10.1016/j.arth.2016.07.027.
- [5] S.B. Goodman, Z. Yao, M. Keeney, F. Yang, The future of biologic coatings for orthopaedic implants, Biomaterials 34 (2013) 3174–3183, https://doi.org/ 10.1016/j.biomaterials.2013.01.074.
- [6] B.D. Ulery, L.S. Nair, C.T. Laurencin, Biomedical applications of biodegradable polymers, J. Polym. Sci. Part B: Polym. Phys. 49 (2011) 832–864, https://doi.org/ 10.1002/polb.22259.
- [7] H. Liu, E.B. Slamovich, T.J. Webster, Less harmful acidic degradation of poly (lactic-co-glycolic acid) bone tissue engineering scaffolds through titania nanoparticle addition, Int. J. Nanomed. 1 (2006) 541–545, https://doi.org/ 10.2147/nano.2006.1.4.541.
- [8] D. Zhao, S. Huang, F. Lu, B. Wang, L. Yang, L. Qin, K. Yang, Y. Li, W. Li, W. Wang, Vascularized bone grafting fixed by biodegradable magnesium screw for treating osteonecrosis of the femoral head, Biomaterials 81 (2016) 84–92, https://doi.org/ 10.1016/j.biomaterials.2015.11.038.
- [9] H. Windhagen, K. Radtke, A. Weizbauer, J. Diekmann, Y. Noll, U. Kreimeyer, R. Schavan, C. Stukenborg-Colsman, H. Waizy, Biodegradable magnesium-based screw clinically equivalent to titanium screw in hallux valgus surgery: short term results of the first prospective, randomized, controlled clinical pilot study, Biomed. Eng. Online 12 (2013) 62–71, https://doi.org/10.1186/1475-925X-12-62.
- [10] J.W. Lee, H.S. Han, K.J. Han, J. Park, H. Jeon, M.R. Ok, H.K. Seok, J.P. Ahn, K. E. Lee, D.H. Lee, Long-term clinical study and multiscale analysis of in vivo biodegradation mechanism of Mg alloy, Proc. Natl. Acad. Sci. USA 113 (2016) 716–721, https://doi.org/10.1073/pnas.1518238113.
- [11] U. Thormann, V. Alt, L. Heimann, C. Gasquere, C. Heiss, G. Szalay, J. Franke, R. Schnettler, K.S. Lips, The biocompatibility of degradable magnesium interference screws: an experimental study with sheep, BioMed Res. Int. 2015 (2015) 1–15, https://doi.org/10.1155/2015/943603.
- [12] H. Yang, B. Jia, Z. Zhang, X. Qu, G. Li, W. Lin, D. Zhu, K. Dai, Y. Zheng, Alloying design of biodegradable zinc as promising bone implants for load-bearing applications, Nat. Commun. 11 (2020) 401, https://doi.org/10.1038/s41467-019-14152.7
- [13] Z.J. Ma, M. Yamaguchi, Alternation in bone components with increasing age of newborn rats: Role of zinc in bone growth, J. Bone Miner. Metab. 18 (2000) 264–270
- [14] H.J. Seo, Y.E. Cho, T. Kim, H.I. Shin, I.S. Kwun, Zinc may increase bone formation through stimulating cell proliferation, alkaline phosphatase activity and collagen synthesis in osteoblastic MC3T3-E1 cells, Nutr. Res. Pract. 4 (2010) 356–361, https://doi.org/10.4162/nrp.2010.4.5.356.
- [15] P. Clément-Lacroix, M. Ai, F. Morvan, S. Roman-Roman, B. Vayssière, C. Belleville, K. Estrera, M.L. Warman, R. Baron, G. Rawadi, Lrp5-independent activation of Wnt signaling by lithium chloride increases bone formation and bone mass in mice, Proc. Natl. Acad. Sci. USA 102 (2005) 17406, https://doi.org/10.1073/ pnas.0505255102
- [16] J. Li, Z. Khavandgar, S.-H. Lin, M. Murshed, Lithium chloride attenuates BMP-2 signaling and inhibits osteogenic differentiation through a novel WNT/GSK3-independent mechanism, Bone 48 (2011) 321–331, https://doi.org/10.1016/j.bone.2010.09.033.
- [17] M. Laroche, V. Lamboley, J.M. Amigues, A. Cantagrel, B. Mazières, Hyperparathyroidism during lithium therapy. Two new cases, Rev. Rhum. 64 (1997) 132–134.
- [18] A. Pelton, The Li-Zn (lithium-zinc) system, J. Phase Equilib. 12 (1991) 42-45.
- [19] S.J. Park, S.H. Kim, H.S. Choi, Y. Rhee, S.K. Lim, Fibroblast growth factor 2-induced cytoplasmic asparaginyl-tRNA synthetase promotes survival of osteoblasts by regulating anti-apoptotic PI3K/Akt signaling, Bone 45 (2009) 994–1003.
- [20] M. Mittal, S. Pal, S.P. China, K. Porwal, K. Dev, R. Shrivastava, K.S.R. Raju, M. Rashid, A.K. Trivedi, S. Sanyal, Pharmacological activation of aldehyde dehydrogenase 2 promotes osteoblast differentiation via bone morphogenetic protein-2 and induces bone anabolic effect, Toxicol. Appl. Pharmacol. 316 (2017) 63–73, https://doi.org/10.1016/j.taap.2016.12.013.
- [21] F. Rauch, F.H. Glorieux, Osteogenesis imperfecta, Lancet 363 (2004) (2004) 1377–1385, https://doi.org/10.1016/S0140-6736(04)16051-0.
- [22] M. Francis, A. Grider, MiRNA-target interactions in osteogenic signaling pathways involving zinc via the metal regulatory element, Biometals 32 (2019) 111–121, https://doi.org/10.1007/s10534-018-00162-4.

- [23] A.W. Holle, A.J. McIntyre, J. Kehe, P. Wijesekara, J.L. Young, L.G. Vincent, A. J. Engler, High content image analysis of focal adhesion-dependent mechanosensitive stem cell differentiation, Integr. Biol. 8 (2016) 1049–1058, https://doi.org/10.1039/c6ib00076b.
- [24] M. Nagata, B. Lönnerdal, Role of zinc in cellular zinc trafficking and mineralization in a murine osteoblast-like cell line, J. Nutr. Biochem. 22 (2011) 172–178, https://doi.org/10.1016/j.jnutbio.2010.01.003.
- [25] S. Shao, H. Fang, L. Duan, X. Ye, S. Rao, J. Han, Y. Li, G. Yuan, W. Liu, X. Zhang, Lysyl hydroxylase 3 increases collagen deposition and promotes pulmonary fibrosis by activating TGFβ1/Smad3 and Wnt/β-catenin pathways, Arch. Med. Sci. 16 (2020) 436–445, https://doi.org/10.5114/aoms.2018.81357.
- [26] A.I. Alford, S.P. Terkhorn, A.B. Reddy, K.D. Hankenson, Thrombospondin-2 regulates matrix mineralization in MC3T3-E1 pre-osteoblasts, Bone 46 (2010) 464–471, https://doi.org/10.1016/j.bone.2009.08.058.
- [27] A.M. Layton, E.A. Eady, D.M. Thiboutot, J. Tan, Identifying what to measure in acne clinical trials: First steps towards development of a core outcome set, J. Invest. Dermatol. 137 (2017) 1784–1786, https://doi.org/10.1016/j. iid/2017/04.017
- [28] M.Z. Liu, D.C. Zhou, Q. Liu, F.L. Xie, D.X. Xiang, G.Y. Tang, S.L. Luo, Osteogenesis activity of isocoumarin a through the activation of the PI3K-Akt/Erk cascadeactivated BMP/RUNX2 signaling pathway, Eur. J. Pharmacol. 858 (2019), 172480, https://doi.org/10.1016/j.ejphar.2019.172480.
- [29] N.J. Lakhkar, I.H. Lee, H.W. Kim, V. Salih, I.B. Wall, J.C. Knowles, Bone formation controlled by biologically relevant inorganic ions: role and controlled delivery from phosphate-based glasses, Adv. Drug Deliv. Rev. 65 (2013) 405–420, https:// doi.org/10.1016/j.addr.2012.05.015.
- [30] J. Wei, J. Shimazu, M.P. Makinistoglu, A. Maurizi, D. Kajimura, H. Zong, T. Takarada, T. Iezaki, J.E. Pessin, E. Hinoi, Glucose uptake and Runx2 synergize to orchestrate osteoblast differentiation and bone formation, Cell 161 (2015) 1576–1591, https://doi.org/10.1016/j.cell.2015.05.029.
- [31] F. Zivic, S. Affatato, M. Trajanovic, M. Schnabelrauch, N. Grujovic, K.L. Choy, Biomaterials in Clinical Practice: Advances in Clinical Research and Medical Devices. Springer. 2017.
- [32] G. Reith, V. Schmitz-Greven, K.O. Hensel, M.M. Schneider, T. Tinschmann, B. Bouillon, C. Probst, Metal implant removal: benefits and drawbacks-a patient survey, BMC Surg. 15 (2015) 96–103, https://doi.org/10.1186/s12893-015-0081-
- [33] N.S. Moghaddam, M.T. Andani, A. Amerinatanzi, C. Haberland, S. Huff, M. Miller, M. Elahinia, D. Dean, Metals for bone implants: Safety, design, and efficacy, Biomanuf. Rev. 1 (2016) 1–16, https://doi.org/10.1007/s40898-016-0001-2.
- [34] Y.F. Zheng, X.N. Gu, F. Witte, Biodegradable metals, Mater. Sci. Eng. R-Rep. 77 (2014) 1–34, https://doi.org/10.1016/j.mser.2014.01.001.
- [35] Y. Liu, Y. Zheng, X.H. Chen, J.A. Yang, H. Pan, D. Chen, L. Wang, J. Zhang, D. Zhu, S. Wu, Fundamental theory of biodegradable metals—definition, criteria, and design, Adv. Funct. Mater. 1805402 (2019), https://doi.org/10.1002/ adfm.201805402.

- [36] Y. Onuma, P.W. Serruys, Bioresorbable Scaffolds: From Basic Concept to Clinical Applications, CRC Press, 2017.
- [37] M.P. Staiger, A.M. Pietak, J. Huadmai, G. Dias, Magnesium and its alloys as orthopedic biomaterials: A review, Biomaterials 27 (2006) 1728–1734, https://doi. org/10.1016/j.biomaterials.2005.10.003.
- [38] R. Gorejová, L. Haverová, R. Oriňaková, A. Oriňak, M. Oriňak, Recent advancements in Fe-based biodegradable materials for bone repair, J. Mater. Sci. 54 (2019) 1913–1947, https://doi.org/10.1007/s10853-018-3011-z.
- [39] G. Li, H. Yang, Y. Zheng, X.H. Chen, J.-A. Yang, D. Zhu, L. Ruan, K. Takashima, Challenges in the use of zinc and its alloys as biodegradable metals: perspective from biomechanical compatibility, Acta Biomater. 97 (2019) 23–45, https://doi. org/10.1016/j.actbio.2019.07.038.
- [40] F. Witte, V. Kaese, H. Haferkamp, E. Switzer, A. Meyer-Lindenberg, C. Wirth, H. Windhagen, In vivo corrosion of four magnesium alloys and the associated bone response, Biomaterials 26 (2005) 3557–3563, https://doi.org/10.1016/j. biomaterials.2004.09.049.
- [41] L. Tian, N. Tang, T. Ngai, C. Wu, Y. Ruan, L. Huang, L. Qin, Hybrid fracture fixation systems developed for orthopaedic applications: A general review, J. Orthop. Transl. 16 (2019) 1–13, https://doi.org/10.1016/j.jot.2018.06.006.
- [42] Y. Zhang, J. Xu, Y.C. Ruan, M.K. Yu, M. O'Laughlin, H. Wise, et al., Implantderived magnesium induces local neuronal production of CGRP to improve bone-fracture healing in rats, Nat. Med. 22 (10) (2016) 1160–1169, https://doi.org/10.1038/ nm.4162.
- [43] L. Tian, Y. Sheng, L. Huang, D.H.K. Chow, W.H. Chau, N. Tang, T. Ngai, C. Wu, J. Lu, L. Qin, An innovative Mg/Ti hybrid fixation system developed fr fracture fixation and healing enhancement at load-bearing skeletal site, Biomaterials 180 (2018) 173–183, https://doi.org/10.1016/j.biomaterials.2018.07.018.
- [44] Z. Li, Z. Shi, Y. Hao, H. Li, H. Zhang, X. Liu, L. Wang, Insight into role and mechanism of Li on the key aspects of biodegradable ZnLi alloys: Microstructure evolution, mechanical properties, corrosion behavior and cytotoxicity, Mater. Sci. Eng., C, 114 (2020) 111049, https://doi.org/10.1016/j.msec.2020.111049.
- [45] Z. Li, Z. Shi, Y. Hao, H. Li, X. Liu, A.A. Volinsky, H. Zhang, L. Wang, High-performance hot-warm rolled Zn-0.8 Li alloy with nano-sized metastable precipitates and sub-micron grains for biodegradable stents, J. Mater. Sci. Technol. 35 (2019) 2618–2624, https://doi.org/10.1016/j.jmst.2019.06.009.
- [46] K.B. Hadley, S.M. Newman, J.R. Hunt, Dietary zinc reduces osteoclast resorption activities and increases markers of osteoblast differentiation, matrix maturation, and mineralization in the long bones of growing rats, J. Nutr. Biochem. 21 (4) (2010) 297–303, https://doi.org/10.1016/j.jnutbio.2009.01.002.
- [47] B.S. Moonga, D.W. Dempster, Zinc is a potent inhibitor of osteoclastic bone resorption in vitro, J. Bone Miner. Res. 10 (1995) 453–457, https://doi.org/ 10.1002/jbmr.5650100317.
- [48] J.L. Wang, J.K. Xu, C. Hopkins, D.H.K. Chow, L. Qin, Biodegradable magnesium-based Implants in orthopedics—A general review and perspectives, Adv. Sci. 7 (2020) 1902443, https://doi.org/10.1002/advs.201902443.
- [49] S.S. Gropper, J.L. Smith, Advanced nutrition and human metabolism, Cengage Learning, ed. 6, 2012.